

ARTICLE

DOI: 10.1038/s41467-017-02003-3

OPEN

Magnetostriction-polarization coupling in multiferroic Mn_2MnWO_6

Man-Rong Li^{1,2}, Emma E. McCabe³, Peter W. Stephens⁴, Mark Croft⁵, Liam Collins⁶, Sergei V. Kalinin⁶, Zheng Deng², Maria Retuerto², Arnab Sen Gupta⁷, Haricharan Padmanabhan⁷, Venkatraman Gopalan⁷, Christoph P. Grams⁸, Joachim Hemberger⁸, Fabio Orlandi⁹, Pascal Manuel⁹, Wen-Min Li¹⁰, Chang-Qing Jin¹⁰, David Walker¹¹ & Martha Greenblatt²

Double corundum-related polar magnets are promising materials for multiferroic and magnetoelectric applications in spintronics. However, their design and synthesis is a challenge, and magnetoelectric coupling has only been observed in Ni_3TeO_6 among the known double corundum compounds to date. Here we address the high-pressure synthesis of a new polar and antiferromagnetic corundum derivative Mn_2MnWO_6 , which adopts the Ni_3TeO_6 -type structure with low temperature first-order field-induced metamagnetic phase transitions ($T_N = 58\text{ K}$) and high spontaneous polarization ($\sim 63.3\ \mu\text{C}\cdot\text{cm}^{-2}$). The magnetostriction-polarization coupling in Mn_2MnWO_6 is evidenced by second harmonic generation effect, and corroborated by magnetic-field-dependent pyroresponse behavior, which together with the magnetic-field-dependent polarization and dielectric measurements, qualitatively indicate magnetoelectric coupling. Piezoresponse force microscopy imaging and spectroscopy studies on Mn_2MnWO_6 show switchable polarization, which motivates further exploration on magnetoelectric effect in single crystal/thin film specimens.

¹Key Laboratory of Bioinorganic and Synthetic Chemistry of Ministry of Education, School of Chemistry, Sun Yat-Sen University, Guangzhou 510275, P. R. China. ²Department of Chemistry and Chemical Biology, Rutgers, the State University of New Jersey, 610 Taylor Road, Piscataway, NJ 08854, USA. ³School of Physical Sciences, University of Kent, Canterbury, Kent CT2 7NH, UK. ⁴Department of Physics & Astronomy, State University of New York, Stony Brook, NY 11794, USA. ⁵Department of Physics and Astronomy, Rutgers, the State University of New Jersey, 136 Frelinghusen Road, Piscataway, NJ 08854, USA. ⁶Centre for Nanophase Material Science & Institute for Functional Imaging of Materials, Oak Ridge National Laboratory, Oak Ridge, TN 37831, USA. ⁷Department of Materials Science and Engineering, Pennsylvania State University, University Park, PA 16802, USA. ⁸II Physikalisches Institut, Universität zu Köln, D 50937 Köln, Germany. ⁹ISIS facility, STFC, Rutherford Appleton Laboratory, Chilton, Didcot, Oxfordshire OX11 0QX, UK. ¹⁰Institute of Physics, Chinese Academy of Sciences, P. O. Box 603, Beijing 100080, China. ¹¹Lamont Doherty Earth Observatory, Columbia University, 61 Route 9W, PO Box 1000, Palisades, NY 10964, USA. Correspondence and requests for materials should be addressed to M.-R.L. (email: limanrong@mail.sysu.edu.cn) or to M.G. (email: greenbla@chem.rutgers.edu)

The structural features of corundum derivatives provide an ideal platform for designing polar and magnetic compounds, since magnetic ions can be incorporated into both the octahedral *A*- and *B*-sites to lead to strong magnetic interactions, accompanied by large spontaneous polarization (P_S) if the polar LiNbO₃ (LN, *R3c*), ordered ilmenite (OIL, *R3*), or Ni₃TeO₆ (NTO, *R3*) type structure is adopted^{1–14}. Remarkable physical properties, such as multiferroic, piezoelectric, pyroelectric and second harmonic generation (SHG) effect, have been demonstrated in these materials. For example, the coexistence of weak ferromagnetism and ferroelectricity has been observed in the high-pressure LN-type FeTiO₃ and in recently-reported GaFeO₃^{2, 14}, and non-hysteretic colossal magnetoelectricity was found in collinear antiferromagnetic (AFM) NTO, which is, to the best of our knowledge, the only experimentally observed magnetoelectric coupling in the double corundum family⁵. In contrast to the off-centering displacement of d^0 *B* cations in the octahedra occurring in many ferroelectric perovskites^{15–17}, in corundum-type *ABO*₃ or *A₂BB'O*₆ materials, the polarization reversal is driven by the small *A* or *B* cations moving between oxygen octahedra^{18, 19}, hence the d^0 configuration is not required. Therefore, considering the potential combinations of *A*1, *A*2, *B*, and *B'* in the (*A*1*A*2)*BB'O*₆ corundum family (where *A*1, *A*2, and *B*, or any two of them could be the same element, or all cations could be different), a very large number of new multifunctional materials are anticipated with the assistance of high pressure (HP) synthesis techniques. However, to the best of our knowledge, only 14 polar and magnetic *A₂BB'O*₆-type corundum-related compounds have been reported to date (see Supplementary Table 1); of these, 11 compounds were experimentally prepared: Ni₃TeO₆^{5, 20}, Ni₂ScSbO₆³, and Ni₂InSbO₆³ were synthesized at ambient pressure, while the rest can only be stabilized at HP. Zn₂FeOsO₆²¹ and A₂FeMoO₆ (*A* = Sc, Lu)²² have only been predicted by first principle calculations to show considerable large P_S .

In this work, we present the HP synthesis of a new polar and magnetic compound Mn₂MnWO₆ (Mn^{*A*}₂Mn^{*B*}W^{*B'*}O₆), which is predicted by first principles calculations to show switchable polarization in an anticipated ferrimagnetic ground state^{23, 24}. The crystal and magnetic structures, cationic oxidation states as well as the physical properties, including second harmonic generation (SHG), magnetic properties, piezo-, pyro-, ferroelectric and magnetoelectric responses, are extensively studied.

Results

Crystal structure of Mn₂MnWO₆. Earlier, Mn₂MnWO₆ single crystals prepared by CO₂-LASER technique in H₂-atmosphere at ambient pressure were reported with the Mg₃TeO₆-type structure (Supplementary Fig. 1)²⁵. The Mn₂MnWO₆ polymorph we report here, prepared at 1673 K and 8 GPa (see Methods), forms in a different crystal structure. Synchrotron powder x-ray diffraction (SPXD) and neutron powder diffraction (NPD) data collected on the as-made sample indicate a rhombohedral (*R3*, No. 146) majority phase with a small impurity. The phases were identified as a NTO-type Mn₂MnWO₆ main phase ($a = 5.32323(3)$ Å, $c = 14.0589(1)$ Å, $V = 345.01(1)$ Å³) and ~ 3.3(1) wt %-MnWO₄ wolframite^{26, 27}, from combined Rietveld refinements of SPXD and NPD data (Supplementary Fig. 2, $R_p/R_{wp} = 4.74/4.55\%$, $\chi^2 = 3.67$). All the cation sites were set as fully occupied, since free refinements lead to less than 1% deviation. There is good contrast between Mn and W neutron scattering lengths (Mn = -3.73 fm, W = 4.86 fm)²⁸ and allowing Mn - W antisite disorder (with constraints to maintain stoichiometry) in combined SPXD and NPD refinements suggested no disorder (antisite occupancies refined to < 1% with no improvement in fit). The final refinement

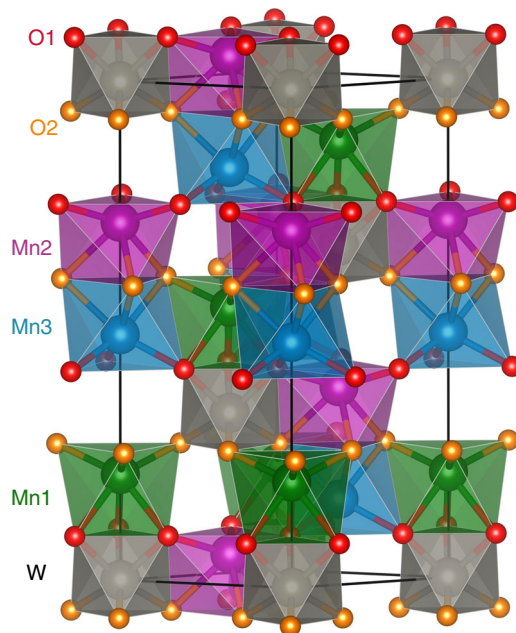


Fig. 1 Crystal structure of Mn₂MnWO₆. The three-dimensional framework structure of Mn₂MnWO₆ viewed along [110] direction, to show the face-sharing Mn1O₆-WO₆ and Mn2O₆-Mn3O₆ octahedral pairs along the *c*-axis and the edge-sharing Mn1O₆-Mn3O₆ and Mn2O₆-WO₆ octahedral pairs in the *ab*-plane. The color codes of spheres are corresponding to Mn1-green, Mn2-purple, Mn3-cyan; W-light gray, O1-red, and O2-orange

results are listed in Supplementary Table 2 and the crystal structure is shown in Fig. 1. Mn₂MnWO₆ is isostructural with Mn₂FeWO₆ and crystallizes in NTO-structure with three independent Mn- (Mn1, Mn2, and Mn3), one W-, and two oxygen sites (O1 and O2), giving the structural formula of (Mn1Mn2)^{*A*}Mn3^{*B*}W^{*B'*}O₆. The face-sharing Mn1O₆-WO₆ and Mn2O₆-Mn3O₆ octahedral pairs are arranged alternatively along the *c*-axis and separated by octahedral vacancies. In the *ab*-plane, the edge-sharing Mn1O₆-Mn3O₆ and Mn2O₆-WO₆ octahedral layers are connected alternatively to form a framework structure (see Fig. 1).

The paired face-sharing arrangement yields high octahedral distortions as reflected by the octahedral distortion parameter (Δ_M)²⁹ and atomic displacement (d_M , distance between cation and its octahedral centroid) along the *c*-axis (Supplementary Table 3). The largest Δ and d values are observed at the Mn2 site with $\Delta_{Mn2} = 5.07 \times 10^{-3}$, $d_{Mn2} = 0.517$ Å, which are very comparable to those of the Mn2 site (5.45×10^{-3} and 0.544 Å) in the Mn₂FeWO₆ analog⁷. These anisotropic atomic displacements induce a large P_S (e.g. $63.3 \mu\text{C}\cdot\text{cm}^{-2}$ at 290 K, as estimated by the point-charge displacement model)^{30, 31}, and give three long and three short metal-oxygen bond distances for each octahedron, varying from 2.061(1) to 2.377(2) Å for Mn-O and 1.867(2) to 1.999(1) Å for W-O. The average < Mn-O > distance lies between 2.196(2) and 2.217(2) Å, comparable to the < Mn-O > of 2.187(9) and 2.228(6) Å for Mn1 and Mn2 in Mn₂FeWO₆. The < W-O > value 1.933(9) Å is close to the < W-O > (1.925(9) Å) in Mn₂FeWO₆⁷. Bond valance sums (BVS) calculations^{29, 32–34} give + 2.00, + 2.06, + 2.09, and + 5.84 for Mn1, Mn2, Mn3, and W, respectively, supporting formal cationic oxidation states of Mn²⁺₂Mn²⁺W⁶⁺O₆ and well accounting for its slightly larger unit cell volume ($345.01(1)$ Å³, $r(VI\text{Mn}^{2+}) = 0.83$ Å) than that of the isostructural Mn²⁺₂Fe²⁺W⁶⁺O₆ ($338.65(1)$ Å³, $r(VI\text{Fe}^{2+}) = 0.78$ Å)³⁵. The large difference in ionic size and charge between Mn²⁺ and W⁶⁺ is

also responsible for the absence of anti-site disordering. The proposed formal cation oxidation states have been further evidenced by the x-ray absorption near edge spectroscopy (XANES) studies (Supplementary Figs. 3–5).

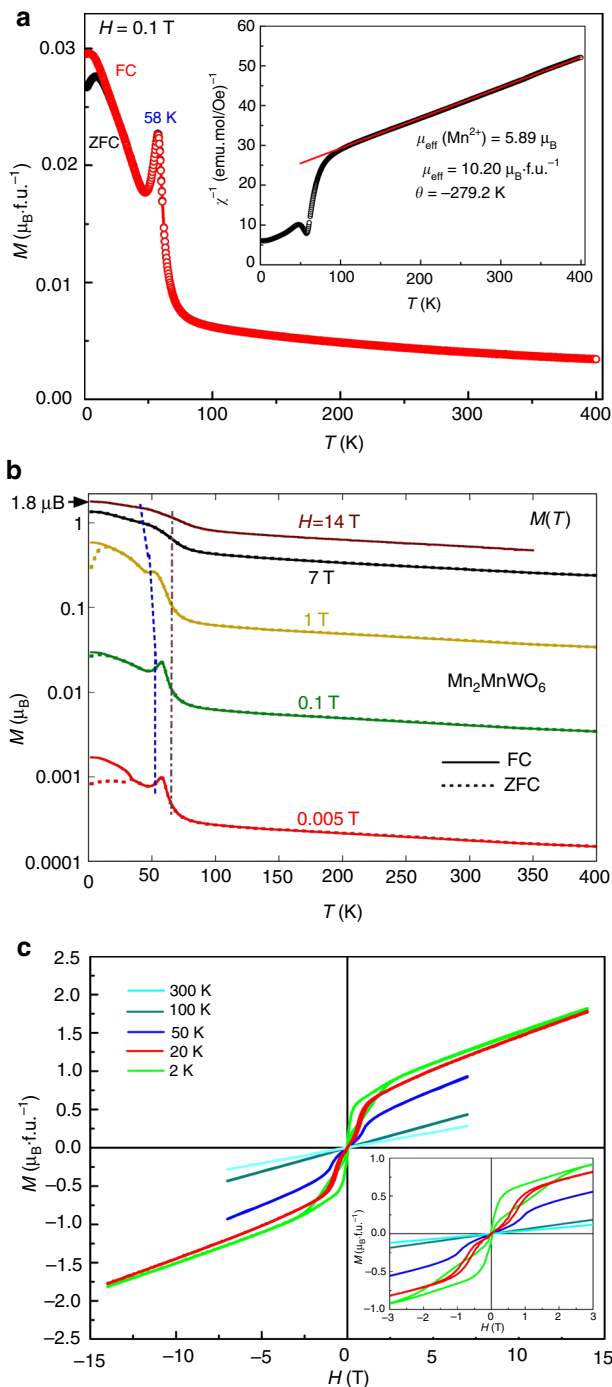


Fig. 2 Magnetic properties of Mn_2MnWO_6 . **a** Thermal evolution of the ZFC and FC mode magnetization (M) and the reciprocal susceptibility (inset) of Mn_2MnWO_6 measured with $H = 0.1 \text{ T}$ up to 400 K. **b** A logarithmic plot of the $M(T)$ curves at a series of magnetic fields between 0.005 and 14 T. The dashed line highlights the evolution of AFM transition temperatures. The dash-dot line highlights the presence of local magnetic correlations near 60 K in all finite magnetic fields. **c** Isothermal magnetization curves of Mn_2MnWO_6 measured at 2, 20, 50, 100, and 300 K between -14 and 14 T for 2 and 20 K; -7 and 7 T for 50, 100, and 300 K. Inset shows the curves between -3 and 3 T

Magnetic properties of Mn_2MnWO_6 . The temperature-dependent magnetization $M(T)$ curves up to 400 K at 0.1 T (Fig. 2a) show that upon cooling the magnetization is enhanced below 80 K and a sharp AFM transition occurs at $\sim 58 \text{ K}$. Below 20 K, the zero-field cooling (ZFC) and field-cooling (FC) curves diverge, indicating a small ferromagnetic component or canted spins in an anisotropic system along with domain effects. At higher temperatures, Mn_2MnWO_6 follows the Curie – Weiss (CW) law; the negative Weiss temperature ($\theta = -279.2 \text{ K}$) is much lower than the AFM transition at $T_N \sim 58 \text{ K}$, again suggesting significant magnetic frustration/interaction. The effective magnetic moment (μ_{eff}) derived from the CW fit of $1/\chi(T)$ over the paramagnetic region (inset of Fig. 2a) is $10.20 \mu_B \cdot \text{f.u.}^{-1}$ (f.u. = formula unit), which gives an average value of $5.89 \mu_B \cdot \text{f.u.}^{-1}$ for each Mn site, consistent with the theoretical value ($5.92 \mu_B \cdot \text{f.u.}^{-1}$) of high-spin $d^5\text{-Mn}^{2+}$ state. Figure 2b shows the logarithmic- $M(T)$ curves collected in both ZFC and FC modes between 0.005 and 14 T up to 400 K. Below 1 T, the $M(T)$ plots manifest robust AFM transitions $\sim 58 \text{ K}$ as evidenced by: the inflection point (below the peak) in the $M(T)$ data; the sharp peak in the dM/dT curves shown in Supplementary Fig. 6; and the isothermal $M(H)$ hysteresis loops below 50 K in Fig. 2c and Supplementary Fig. 7. At 1 T, this AFM transition is weakened and moved to lower temperature as highlighted by the dashed line in Fig. 2b and Supplementary Figs. 6 and 8. Above 7 T this AFM order is substantially modified and the detailed character of the high field AFM state is uncertain. The $M(T)$ curves also evidence structure near 60 K at all fields indicating local magnetic correlations on this energy scale. The presence of a low temperature first-order field-induced metamagnetic phase transition (Supplementary Fig. 8), similar to that observed in Mn_2FeWO_6 ⁷, is clear from the isothermal magnetization curves, $M(H)$, shown in Fig. 2c and in expanded views (with additional data) in Supplementary Fig. 7. The magnetization is far from saturation at 2 K and 14 T, and gives a value of only $\sim 1.82 \mu_B \cdot \text{f.u.}^{-1}$, indicating that AFM order still strongly constrains the field response in this regime.

Magnetic structure of Mn_2MnWO_6 . To better understand the magnetic behavior of Mn_2MnWO_6 , NPD data at lower temperatures were recorded. Additional Bragg reflections were observed below $\sim 55 \text{ K}$ with intensity increasing smoothly on cooling (Supplementary Fig. 9). Some magnetic reflections were consistent with a magnetic unit cell commensurate with the nuclear crystal structure with magnetic propagation vector $k_1 = (0 \ 0 \ 3/2)$ (T point of the first Brillouin zone) while other reflections were broader and consistent with an incommensurate modulation with $k_2 \approx (0 \ 0 \ 0.3)$ (Λ line of the first Brillouin zone) (Supplementary Fig. 9). Good fits to the 5 K NPD data were obtained for models of $R_13(00g)t$ symmetry with the magnetic unit cell related to the nuclear cell through the transformation $\{(0-10)(110)(002)\}$. This magnetic superspace symmetry is a result of both the $mT1$ and $m\Lambda 2LE2$ irreps acting on all three manganese sites. Models with only one irrep acting on each site gave poor fits to the data and unphysical moments for Mn^{2+} sites. Various models with AFM ordering of manganese moments along [001] (described by irrep $mT1$) with these moments tilted towards the ab plane rotating around [001] (described by $m\Lambda 2LE2$ irrep), giving Mn moments arranged in cones around [001], gave good fits to the experimental data. Constraints were needed to give a stable refinement and convergence and the z and xy components of the Mn2 moments were constrained to be half and double those of the Mn1/Mn3 sites, respectively. This gives overall moments of $4.2(5)$ and $4.4(5) \mu_B$ for Mn1/Mn3 and Mn2 sites at 5 K, respectively, with incommensurate propagation

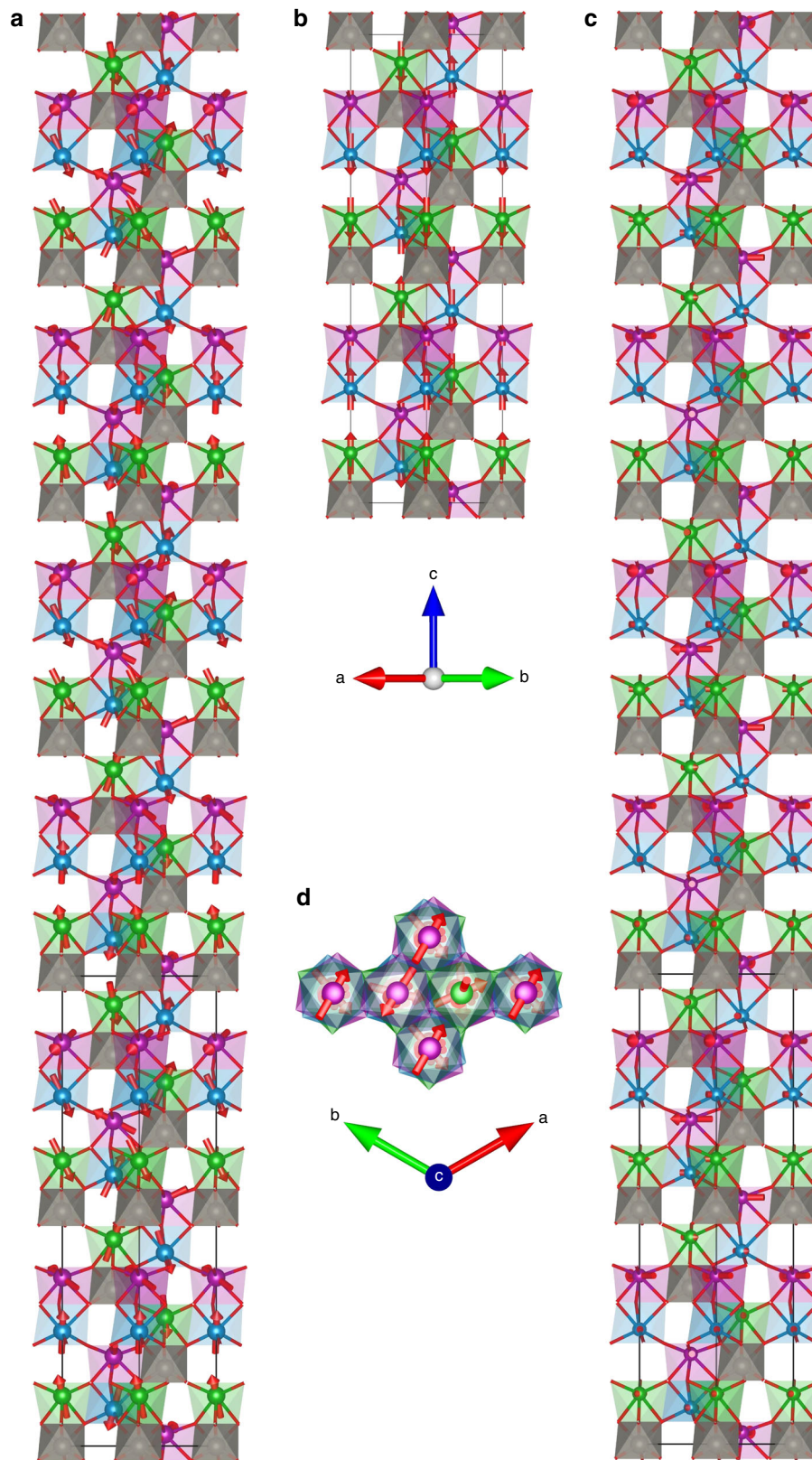


Fig. 3 Illustration of the nuclear and magnetic structures of Mn_2MnWO_6 at 5 K. Mn1, Mn2, Mn3 and W sites and polyhedra are shown in green, purple, blue and grey, respectively, with Mn moments shown by red arrows (color online) (oxide ions are omitted for clarity). **a** shows the complete magnetic structure (showing six times the nuclear unit cell along c). **b** shows only the z component of Mn moments (described by commensurate $m\bar{1}1$ irrep) and **c** shows only the xy component of Mn1 and Mn3 moments (described by $m\bar{1}2LE2$ irrep) (showing six times the nuclear unit cell along c), also **d** showing view down along c axis of magnetic unit cell

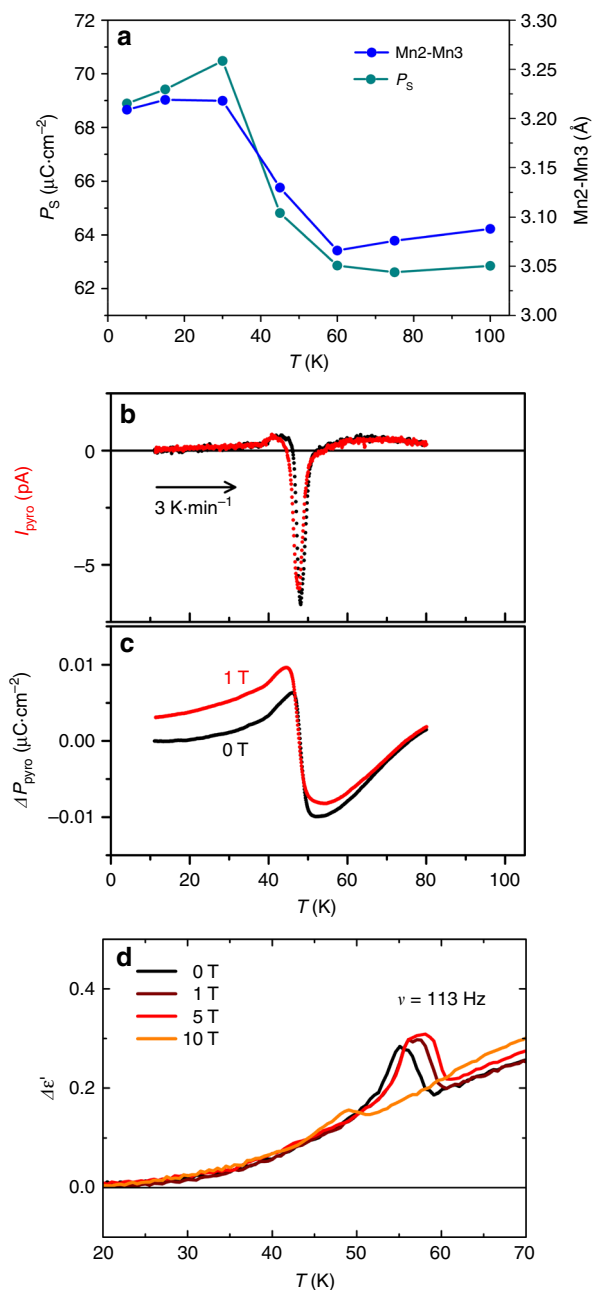


Fig. 4 Magnetostriction-polarization coupling and pyroresponse in Mn_2MnWO_6 . **a** Temperature dependent spontaneous polarization (P_s , calculated) and Mn2-Mn3 distance evolution in Mn_2MnWO_6 between 5 and 100 K. **b** Pyro-current as a function of temperature between 10 and 80 K, and **c** Pyroelectric polarization measured in 0 and 1 T upon warming and normalized to a common high temperature value. **d** Temperature dependent dielectric data between 0 and 10 T show anomalies around T_N and indicate magnetoelectric coupling

vector $k = 0 \ 0 \ 0.6107(8)$ ($k = (0 \ 0 \ 0.305)$) with respect to the nuclear unit cell). We cannot rule out the possibility of similar magnetic structures giving equally good fits to the data, but the constraints imposed give almost equal moments for each manganese site and across the magnetic structure as might be expected for this insulating oxide. The magnetic and crystal structures at 5 K are shown in Fig. 3 and refinement profiles in Supplementary Fig. 10. Refinement details and selected bond lengths and distances are given in Supplementary Tables 4 and 5. Similar refinements were then carried out using short NPD scans

collected at selected temperatures on warming (with no magnetic component included above T_N).

This zero-field magnetic structure can be described as a superposition of commensurate AFM ordering along [001] (mT1 irrep) and a helical component in the xy plane (m Λ 2LE2 irrep) giving rise to the conical-AFM magnetic structure propagating along [001]. This magnetic structure can be thought of in terms of AFM coupling between Mn1 and Mn3 sites within the Mn1Mn3O_3 layers, with moments predominantly along [001]. The Mn2 moments are predominantly within the (001) planes in the opposite direction to the in-plane component in the Mn1Mn3O_3 layer directly above (this in-plane component is cancelled by that of other layers in the overall magnetic unit cell in this zero-field AFM structure). Manganese moments increase smoothly on cooling (Supplementary Figs. 11 and 12). The AFM arrangement of Mn1 and Mn3 moments predominantly along [001] within the Mn1Mn3O_3 layers satisfies the 90° superexchange interactions expected to be AFM³⁶. The Mn2 site is magnetically coupled to this Mn1Mn3O_3 layer via $\sim 120^\circ$ Mn1 – O2 – Mn2 interactions and $\sim 86^\circ$ Mn3 – O2 – Mn2 interactions across the shared face. Both these exchange interactions are likely to be AFM leading to magnetic frustration, consistent with magnetic susceptibility measurements described above. This frustration is somewhat relieved by the incommensurate modulation that reorients the moments away from [001], particularly for the Mn2 site, allowing its in-plane component to be oriented antiparallel to the in-plane component in the nearest Mn1Mn3O_3 layer (which lies directly above).

Magnetostriction-polarization coupling and magnetoelectric effect in Mn_2MnWO_6 . The unit cell volume of Mn_2MnWO_6 decreases smoothly on cooling until the lowest temperatures when slight negative thermal expansion is observed (Supplementary Fig. 13). This is due to expansion of the unit cell along the [001] direction below T_N . This expansion is thought to be due to magnetostriction across the Mn2 – Mn3 face-shared polyhedra: the Mn2 – Mn3 distance increases below the AFM ordering temperature as the Mn3 site moves towards the O1 layer and away from the O2 layer within the shared face (Fig. 4a and Supplementary Fig. 13), similar to structural changes observed in other materials containing Mn_2O_9 dimers³⁷. This magnetostriction gives a dramatic increase of P_s below T_N , in line with the increase of the Mn2 – Mn3 distance below T_N , giving computed P_s of $62.86 \mu\text{C}\cdot\text{cm}^{-2}$ at 60 K and $70.48 \mu\text{C}\cdot\text{cm}^{-2}$ at 30 K (Fig. 4a and Supplementary Figs. 13 and 14). The coupling between spin structure and the lattice anomalies is well known to play an important role for the observation of multiferroicity³⁸. The magnetostriction-polarization coupling around T_N is also visible in the fluctuation of the SHG intensity (Supplementary Fig. 15). Figure 4b and c show the finite pyrocurrent and pyroelectric polarization response at 0 and 1 T, respectively. A clear anomaly/discontinuity can be detected in the pyrocurrent (Fig. 4b and Supplementary Fig. 16), the pyroelectric polarization (Fig. 4c) and the dielectric (Fig. 4d) curves in the vicinity of the magnetic transition, qualitatively echoed by the magnetostriction effects, which couple the macroscopic polarization of the structure to magnetism. The small difference between pyroresponse at 0 and 1 T suggests possible magnetoelectric coupling, however, one should be aware of experimental uncertainties by lack of a robust effect ($\sim 0.05 \mu\text{C}\cdot\text{cm}^{-2}$ compared with the theoretical value of $\sim 70 \mu\text{C}\cdot\text{cm}^{-2}$ at 20 K) in such a random-distribution polycrystalline specimen as also observed in the magnetic-field-dependent polarization measurement results in Supplementary Fig. 17. However, the temperature-dependent dielectric measurements at several magnetic fields from 0 to 10 T evidence anomalies around

T_N in Fig. 4d. The shift of the transition temperature with the magnetic field as well as the observed suppression in high magnetic fields clearly convince magnetoelectric coupling in Mn_2MnWO_6 .

Switchable polarization of Mn_2MnWO_6 . To further explore the polar and ferroelectric properties of Mn_2MnWO_6 , piezoresponse force microscopy (PFM) imaging and spectroscopic studies were performed at room temperature, since the surface deformation does not depend on the contact radius^{39, 40}, and hence is a direct measure of local piezoelectric properties^{41, 42}. In conjunction with dual amplitude resonance-tracking (DART)⁴³, or band excitation (BE)^{44, 45} modes, PFM allows to obtain quantitative information on material properties. The surface topography and PFM images of a polished sample embedded in epoxy is shown in Supplementary Fig. 18, with clearly visible variation of DART PFM contrast at the grain boundaries, some grains show clearly visible domain structures, highly reminiscent of domain structures for materials such as $BaTiO_3$ ^{46, 47}.

The switching properties of the material were explored with BE PFM polarization spectroscopy measurements⁴⁸. The 750×750 nm region was first imaged by DART PFM as shown in Fig. 5a–c. Representative hysteresis loops of the amplitude and phase are shown in Fig. 5d. The clear hysteresis loops with the characteristic coercive biases of ~ 50 V are observed. Note that the loops are not saturated, suggesting that formation of domains are largely unstable and rapidly relax in the bias-off state. Here, the measurements are performed over rectangular grid of points (35×35), giving rise to the 3D array of hysteresis loops. The latter can be processed to yield 2D maps of materials parameters such as coercive bias of polarization switching. The maps of remnant polarization for positive and negative coercive biases are shown in Fig. 5e and f, which bear some resemblance with underlying domain structure, suggesting the pinning of polarization by preexisting electroelastic fields. The final switching experiment was conducted on the region shown in Supplementary Fig. 19a. In this case, the surface is scanned by a strongly negatively (-100 V) biased tip within a $4 \mu m$ square, and subsequently with a strongly positively biased tip ($+100$ V) within a $2 \mu m$ square (Supplementary Fig. 19d). The polarization distributions after each poling measurement are shown in Supplementary Figs. 19b, c, e, f. Herein, it is conclusive that the polarization in Mn_2MnWO_6 is switchable, as further corroborated by the $P(E)$ loop measurements (Supplementary Fig. 20). For a quantitative image of the ferroelectric and magnetoelectric coupling effect, further exploration on single crystal sample is necessary.

Comparison of Mn_2MnWO_6 and isostructural polar magnets.

It is relevant to compare the magnetic structure of Mn_2MnWO_6 with that of other magnetic NTO materials. In Mn_2ScSbO_6 and Ni_2BSbO_6 ($B = Sc, In$), the non-magnetic ions create holes in the Mn/Ni magnetic sublattices preventing direct exchange between the magnetic sites^{3, 6}. All these systems order AFM, but with no face-shared magnetic M_2O_9 ($M =$ magnetic cation) dimers or magnetic frustration, it is unlikely that magnetostriction-driven changes in polarization occur. However, it is interesting that without nearest-neighbor exchanges, Ni_2BSbO_6 ($B = Sc, In$) is significantly more frustrated than Ni_3TeO_6 and adopts a non-collinear, helical magnetic structure with components of the Ni^{2+} moments along both the c direction and in the ab plane³. NTO systems with three magnetic cations include Mn_2FeWO_6 ⁷, Mn_2FeMoO_6 ⁴, and Ni_3TeO_6 ^{5, 49–52} and exhibit complex magnetic behavior. All three materials differ from Mn_2MnWO_6 (described here) in that they are reported to have collinear magnetic

structures with FM coupling between edge-shared magnetic sites within layers^{49, 50}. The chiral, polar material Ni_3TeO_6 ⁵¹ has been the most thoroughly characterized and it is useful to compare its behavior with that of Mn_2MnWO_6 . Theoretical studies on Ni_3TeO_6 suggest that edge-linked Ni1 and Ni2 sites are coupled FM (J_1) and that face-linked Ni2 and Ni3 sites are also coupled FM (J_2). AFM J_3 , J_4 and J_5 interactions couple the Ni3 site (analogous to the Mn2 site in Mn_2MnWO_6) to Ni1 and Ni2 sites in adjacent layers via corner-linked exchange; the relative strengths of these exchange interactions results in a small degree of frustration, and the experimentally observed (zero-field) magnetic structure is collinear with Ni^{2+} moments oriented along $[001]$ ^{49, 50}.

Mn_2MnWO_6 differs in that the Mn1 – Mn3 coupling between edge-linked sites is AFM. This leads to frustration in the coupling with the Mn2 site through face-shared coupling to Mn3 and corner-linked interactions with Mn1 and Mn3 sites, giving a higher degree of frustration in Mn_2MnWO_6 compared with Ni_3TeO_6 ($|\theta|/T_N \approx 5$ for Mn_2MnWO_6 and ≈ 1 for Ni_3TeO_6 ⁵⁰). This higher level of frustration is likely to give rise to the non-collinear magnetic structure of Mn_2MnWO_6 with a significant in-plane component for the Mn2 moment to somewhat relieve this frustration. Oh et al. reported interesting magnetic field dependent behavior for Ni_3TeO_6 , with an increasing magnetic field along $[001]$ able to switch the system from a higher polarization state to a state with lower polarization⁵. It is interesting that magnetostriction across the face-shared M_2O_9 dimers gives rise to a noticeable change in polarization in both these NTO materials and our variable-temperature NPD experiment allows us to study the magnetic and structural changes through the magnetic phase transition, clearly illustrating this effect (Fig. 4a, Supplementary Figs. 12 and 13). Both Ni_3TeO_6 and Mn_2MnWO_6 are polar as a result of the cation arrangement in this corundum-derived structure type, but the magnetic order modifies the existing electrical polarization^{5, 49–52}. In Mn_2MnWO_6 the magnetic transition is driven by the one dimensional $mT1$ irreducible representation with order parameter μ and by the two dimensional $m\Lambda 2LE2$ with order parameter η_1, η_2 . Since the electrical polarization (P) is already present in the parent structure, it is possible to derive the coupling between the polarization and the magnetic order parameters as the product of P and the magnetic free energy invariant. In this way, the linear quadratic coupling $P(\mu^2 + \eta_1^2 + \eta_2^2)$ is obtained. This coupling term is consistent with the magnetostriction observed experimentally in the neutron diffraction data and is at the basis of the change of the polarization at T_N .

In Ni_3TeO_6 , the field-dependent behavior is ascribed to a spin-flop transition that reorients moments to within the ab plane above a critical field along the polar c axis, H_c ⁵. Field-dependent neutron scattering experiments on the more frustrated Mn_2MnWO_6 (which already has some in-plane component for the moments) would be of interest to understand if a similar explanation might explain the field-dependence observed in magnetic susceptibility measurements (Figs. 2b, c, Supplementary Figs. 7 and 8). Oh et al. describe how applying an electric field along the polar c axis of Ni_3TeO_6 increases the polarization but decreases the magnetization along c ⁵, presumably due to the increased Ni2 – Ni3 separation (which weakens the FM J_2 interaction) and changes the balance between competing J_1, J_2 and J_4 interactions; with in-plane J_1 interactions relatively weak, this may be sufficient to cause reorientation of Ni3 sites as well as Ni1 and Ni2 sites⁵². Single crystal experiments on Mn_2MnWO_6 would be valuable to investigate its (anisotropic) magnetic and dielectric behavior fully. Thus, our combined structural and magnetic study highlights the potential for NTO materials

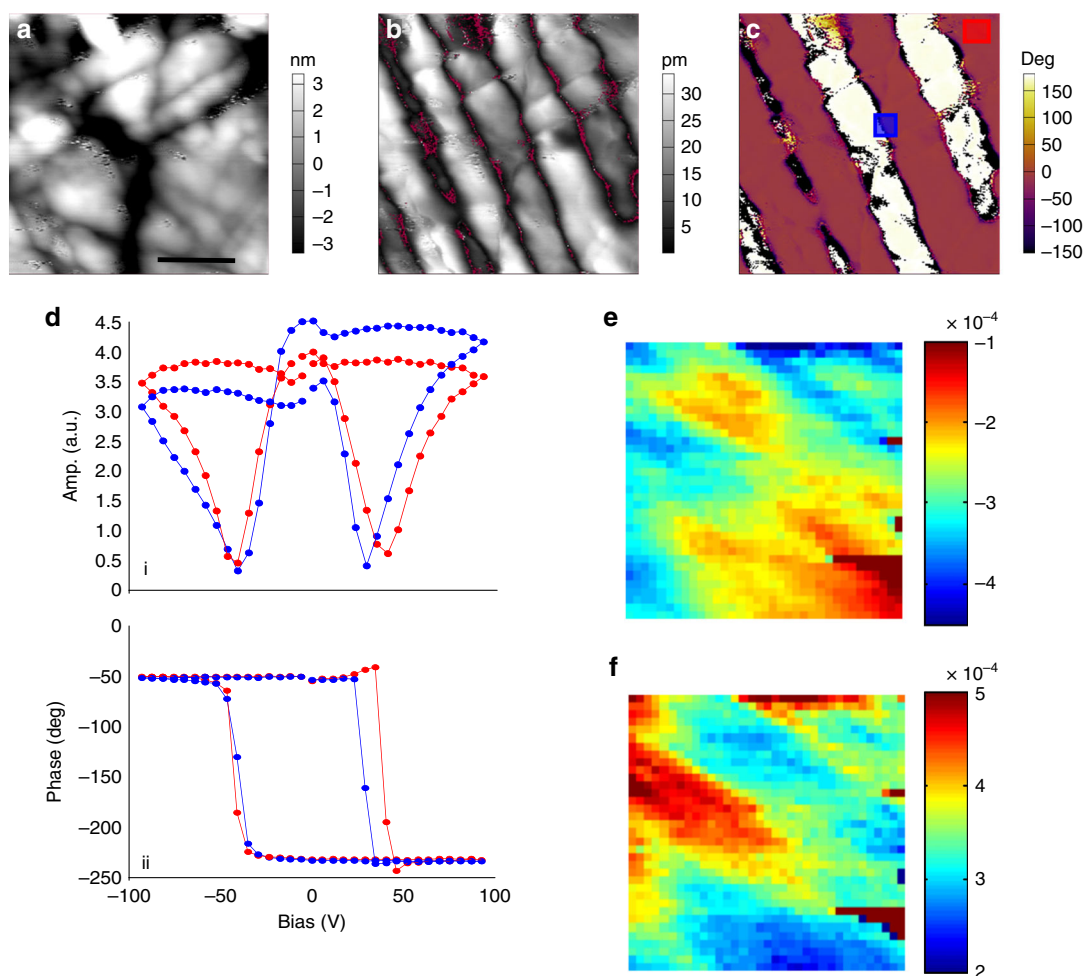


Fig. 5 PFM results on Mn₂MnWO₆. **a** Topography (scale bar 250 nm). **b** PFM DART amplitude and **c** phase. **d** average amplitude (i) and phase (ii) BE PFM switching spectroscopy loops determined from square regions indicated in the phase image in (c). Remnant **e** negative and **f** positive amplitudes determined from fitting 35 × 35 grid measurement. Scale bar is the same for Fig. 5a–c

containing three magnetic cations to exhibit magnetostriction-influenced polarization changes and their complex field dependent behavior warrants further investigation to fully exploit their magnetoelectric coupling.

Discussions

In summary, we have prepared, by high pressure-high temperature techniques, a corundum derivative phase Mn₂MnWO₆, which is a new polar and antiferromagnetic ($P_S \sim 63.3 \mu\text{C}\cdot\text{cm}^{-2}$, $T_N = 58 \text{ K}$) Ni₃TeO₆-type oxide with a low temperature first-order field-induced metamagnetic phase transition. The highly polarized spin structure shows antiferromagnetic coupling with magnetic moments predominantly along [001]. The magnetostriction-polarization coupling around the magnetic transition is echoed by the second harmonic generation effect and further corroborated by pyroresponse behavior with and without magnetic field, which, together with the magnetic-field-dependent polarization measurements, qualitatively indicate magnetoelectric coupling. Piezoresponse force microscopy imaging and spectroscopy studies show that the polarization in Mn₂MnWO₆ is switchable, which motivates further exploration of ferroelectric and magnetoelectric coupling in single crystal and thin film specimens, as well as searching for new polar magnets in the corundum family.

Methods

Synthesis and crystal and magnetic structure determination. Polycrystalline Mn₂MnWO₆ was prepared from a stoichiometric mixture of MnO (99.99%, Alfa Aesar) and WO₃ (99.8%, Alfa Aesar) at 1673 K under 8 GPa for 1 h in a Multi-Anvil Press as used in our previous work^{7–9, 53}. SPXD data were recorded on beam line X-16C ($\lambda = 0.69991 \text{ \AA}$) at the Brookhaven National Synchrotron Light Source. Diffraction data analysis and Rietveld refinement were performed with the TOPAS software package^{54, 55}. NPD data were collected on 0.1063 g sample (placed inside a 3 mm diameter vanadium can with sample height around 4 mm) at the ISIS Neutron source (Rutherford Appleton Laboratory (UK)) on the WISH diffractometer located at the second target station⁵⁶. Data were collected at 290 K (~ 1 h) and then the sample was cooled to 5 K in an Oxford Instruments cryostat and a high quality data set was recorded (~ 3 h). Shorter scans were then collected on warming (~ 35 minute scans in 5 K increments to 80 K, then at 90 and 100 K). Rietveld refinements were carried out with Topas-Academic^{54, 55} (for 290 K data) and Jana2006⁵⁷, for 5 K and intermediate temperature nuclear and magnetic structures). The magnetic symmetry analysis was carried out using ISO-DISTORT⁵⁸. Double-frame data sets were collected at 5 and 100 K to confirm the presence of a magnetic Bragg reflection at ~ 47 Å below T_N . The Mn-K and W-L₃ XANES data were collected in both the transmission and fluorescence mode with simultaneous standards. All of the spectra were fitted to linear pre- and post-edge backgrounds and normalized to unity absorption edge step across the edge^{4, 7, 8, 59, 60}. All of the XANES was performed on beam line X-19A at the Brookhaven National Synchrotron Light Source with a Si-111 double crystal monochromator.

Magnetic properties measurements. Magnetization measurements were carried out with a commercial Quantum Design superconducting quantum interference device (SQUID, up to 7 T) magnetometer and a physical property measurement system (PPMS, up to 14 T). The magnetic susceptibility was measured in zero-field-cooled (ZFC) and field-cooled (FC) conditions under 0.005–14 T magnetic

field, at temperatures ranging from $T = 5\text{--}400\text{ K}$. Isothermal magnetization curves were obtained at $T = 2, 20, 50, 100$ and 300 K under an applied magnetic field that varied from $-14\text{--}14\text{ T}$ for 2 and 20 K and $-7\text{--}7\text{ T}$ for 50, 100, and 300 K . Magnetization curves at additional temperatures and maximum fields are presented in Supplementary Figs. 6 and 7.

SHG measurements. The SHG experiments were performed in the reflection mode on polished pellets (cylinder pellet with 98(1) % of the theoretical density and $\sim 2\text{ mm}$ of diameter and thickness of $\sim 0.3\text{ mm}$) of the as-made polycrystalline Mn_2MnWO_6 . This is a widely used technique for determining noncentrosymmetry in materials^{61–65}. This is an optical technique in which two photons with fields E_j and E_k of frequency ω and directions j and k , respectively, interact with a material with a non-zero d_{ijk} tensor (non-centrosymmetric) forming a polarization $P_i^{2\omega}$ (nonlinear) of frequency 2ω in the i direction. The SHG intensity, $I^{2\omega}$ is detected using a Hamamatsu photo multiplier tube. A Ti-sapphire laser (Spectra-Physics) with an output of 800 nm , 80 fs pulses at 2 kHz frequency was used for this experiment. Temperature scans were performed with an Oxford cryostat ($50\text{--}320\text{ K}$) and a user customized heater ($298\text{--}800\text{ K}$).

Electric measurements. The pyro-current was measured with an electrometer (Keithley 6517) at cooling/heating rates of $1\text{--}3\text{ K}\cdot\text{min}^{-1}$ in a PPMS Cryo-Magnet (Quantum Design); the corresponding polarization data was gained by numerical integration. The ferroelectric P-E loops and magnetic-field dependent polarization measurements were recorded with a modified Sawyer-Tower circuit employing a Keithley 6517 electrometer with linear field ramping at rates of $100\text{ (V}\cdot\text{mm}^{-1})\cdot\text{s}^{-1}$ and $100\text{ Oe}\cdot\text{s}^{-1}$. The samples were sandwiched between Ag paste-deposited electrodes, in parallel plate geometry for the above measurements. It should be noted that due to the use of polycrystalline samples a pyroelectric can only be expected for a not perfectly random distribution of structural domain orientations. Thus the polarization values gained only reflect the qualitative field and temperature dependence and have to be much smaller than the values gained from single crystals or structural refinement. In addition, thermal gradients on the sample may lead via piezo-coupling to finite charge contributions (tertiary pyro-effect) which constitute further uncertainties in the evaluated polarization. The dielectric properties were measured with a NovoControl-Alpha frequency response analyzer.

PFM measurements. In PFM, application of the periodic electric bias to the conductive scanning probe microscopy tip in contact with the surface results in the surface deformation, due to converse piezoelectric effect. This deformation is detected as the periodic deflection of the tip via microscope electronics. This approach has been broadly used for imaging ferroelectric domains in a broad range of ferroelectric and piezoelectric crystals, ceramics, and thin films^{66–70}. The PFM measurements were performed at room temperature with 6 V_{pp} ac bias applied to a Pt/Cr-coated probe (Budget sensors Multi75E-G). For PFM imaging the drive frequency of the ac bias was centred at the contact resonance ($\sim 350\text{ kHz}$) and dual amplitude resonance tracking was then used to track the contact resonance as the tip was scanned across the sample surface⁴³. For the polarization switching experiments a band of frequencies ($\sim 80\text{ kHz}$) centered around the contact resonance frequency were excited, as an additional DC bias was swept from -90 to $+90\text{ V}$. Extraction of the tip parameters were determined from fitting of the response to a simple harmonic oscillator model as described elsewhere^{44, 45}.

Data availability. The data that support the findings of this study are available from the corresponding authors on request.

Received: 2 February 2017 Accepted: 31 October 2017

Published online: 11 December 2017

References

- Woodward, P. M., Sleight, A. W., Du, L.-S. & Grey, C. P. Structural studies and order-disorder phenomenon in a series of new quaternary tellurates of the type $\text{A}^{2+}\text{M}^{4+}\text{Te}^{6+}\text{O}_6$ and $\text{A}^{1+2}\text{M}^{4+}\text{Te}^{6+}\text{O}_6$. *J. Solid State Chem.* **147**, 99–116 (1999).
- Varga, T. et al. Coexistence of weak ferromagnetism and ferroelectricity in the high pressure LiNbO_3 -type phase of FeTiO_3 . *Phys. Rev. Lett.* **103**, 047601 (2009).
- Ivanov, S. A. et al. Spin and dipole ordering in $\text{Ni}_2\text{InSbO}_6$ and $\text{Ni}_2\text{ScSbO}_6$ with corundum-related structure. *Chem. Mater.* **25**, 935–945 (2013).
- Li, M.-R. et al. Magnetic-structure-stabilized polarization in an above-room-temperature ferrimagnet. *Angew. Chem. Int. Ed.* **53**, 10774–10778 (2014).
- Oh, Y. S. et al. Non-hysteretic colossal magnetoelectricity in a collinear antiferromagnet. *Nat. Commun.* **5**, 3201 (2014).
- Solana-Madruga, E. et al. High pressure synthesis of polar and non-polar cation-ordered polymorphs of $\text{Mn}_2\text{ScSbO}_6$. *Dalton Trans.* **44**, 20441–20448 (2015).
- Li, M.-R. et al. Mn_2FeWO_6 : A new Ni_3TeO_6 -type polar and magnetic oxide. *Adv. Mater.* **27**, 2177–2181 (2015).
- Li, M.-R. et al. Designing polar and magnetic oxides: $\text{Zn}_2\text{FeTaO}_6$ - in search of multiferroics. *J. Am. Chem. Soc.* **136**, 8508–8511 (2014).
- Li, M.-R. et al. Polar and magnetic Mn_2FeMO_6 ($\text{M} = \text{Nb, Ta}$) with LiNbO_3 -type Structure: high-pressure synthesis. *Angew. Chem. Int. Ed.* **52**, 8406–8410 (2013).
- Li, M.-R. et al. A polar corundum oxide displaying weak ferromagnetism at room temperature. *J. Am. Chem. Soc.* **134**, 3737–3747 (2012).
- Belik, A. A., Matsushita, Y., Tanaka, M. & Takayama-Muromachi, E. $\text{In}_{1-y}\text{Mn}_y\text{MnO}_3$ ($1/9 \leq y \leq 1/3$): unusual perovskites with unusual properties. *Angew. Chem. Int. Ed.* **49**, 7723–7727 (2010).
- Aimi, A. et al. High-pressure synthesis and correlation between structure, magnetic, and dielectric properties in LiNbO_3 -type MnMO_3 ($\text{M} = \text{Ti, Sn}$). *Inorg. Chem.* **50**, 6392–6398 (2011).
- Rao, C. N. R., Sundaresan, A. & Saha, R. Multiferroic and magnetoelectric oxides: the emerging scenario. *J. Phys. Chem. Lett.* **3**, 2237–2246 (2012).
- Niu, H. et al. Room temperature magnetically ordered polar corundum GaFeO_3 displaying magnetoelectric coupling. *J. Am. Chem. Soc.* **139**, 1520–1531 (2017).
- Spaldin, N. A. A beginner's guide to the modern theory of polarization. *J. Solid State Chem.* **195**, 2–10 (2012).
- Benedek, N. A. & Fennie, C. J. Why are there so few perovskite ferroelectrics? *J. Phys. Chem. C* **117**, 13339–13349 (2013).
- Hill, N. A. Why are there so few magnetic ferroelectrics? *J. Phys. Chem. B* **104**, 6694–6709 (2000).
- Inbar, I. & Cohen, R. E. Comparison of the electronic structures and energetics of ferroelectric LiNbO_3 and LiTaO_3 . *Phys. Rev. B* **53**, 1193–1204 (1996).
- Veithen, M. & Ghosez, P. First-principles study of the dielectric and dynamical properties of lithium niobate. *Phys. Rev. B* **65**, 214302 (2002).
- Becker, R. & Berger, H. Reinvestigation of Ni_3TeO_6 . *Acta Crystallogr. Sect. E* **62**, i222–i223 (2006).
- Wang, P. S., Ren, W., Bellaiche, L. & Xiang, H. J. Predicting a ferrimagnetic phase of $\text{Zn}_2\text{FeOsO}_6$ with strong magnetoelectric coupling. *Phys. Rev. Lett.* **114**, 147204 (2015).
- Song, G. & Zhang, W. Comparative studies on the room-temperature ferroelectric and ferrimagnetic Ni_3TeO_6 -type A_2FeMoO_6 compounds ($\text{A} = \text{Sc, Lu}$). *Sci. Rep.* **6**, 20133 (2016).
- Ye, M. & Vanderbilt, D. Ferroelectricity in corundum derivatives. *Phys. Rev. B* **93**, 134303 (2016).
- Ye, M. & Vanderbilt, D. Domain walls and ferroelectric reversal in corundum derivatives. *Phys. Rev. B* **95**, 014105 (2017).
- Klüver, E. & Müller-Buschbaum, H. Ein neues Mangan(II)-oxowolframat: Mn_3WO_6 . *Z. Anorg. Allg. Chem.* **620**, 733–736 (1994).
- Young, A. P. & Schwartz, C. M. High-pressure synthesis of molybdates with the wolframite structure. *Science* **141**, 348–349 (1963).
- Bish, D. L. & Howard, S. A. Quantitative phase analysis using the Rietveld method. *J. Appl. Crystallogr.* **21**, 86–91 (1988).
- Sears, V. F. *Neutron news* **3**, 29–37 (1990).
- Brown, I. D. & Shannon, R. D. Empirical bond-strength-bond-length curves for oxides. *Acta Crystallogr. Sect. A* **29**, 266–282 (1973).
- Lefevre, C. et al. Magnetic and polar properties' optimization in the magnetoelectric $\text{Ga}_{2-x}\text{Fe}_x\text{O}_3$ compounds. *J. Phys. Chem. C* **117**, 14832–14839 (2013).
- Capillas, C. et al. A new computer tool at the Bilbao Crystallographic Server to detect and characterize pseudosymmetry. *Z. Krist. Cryst. Mater.* **226**, 186–196 (2011).
- Brown, I. D. Recent Developments in the Methods and Applications of the Bond Valence Model. *Chem. Rev.* **109**, 6858–6919 (2009).
- Brese, N. E. & O'Keeffe, M. Bond-valence parameters for solids. *Acta Crystallogr. Sect. B* **47**, 192–197 (1991).
- Lufaso, M. W. & Woodward, P. M. Prediction of the crystal structures of perovskites using the software program SPuDS. *Acta Crystallogr. Sect. B* **57**, 725–738 (2001).
- Shannon, R. Revised effective ionic radii and systematic studies of interatomic distances in halides and chalcogenides. *Acta Crystallogr. Sect. A* **32**, 751–767 (1976).
- Goodenough, J. B. *Magnetism and the chemical bond*. (Wiley, 1963).
- Vente, J. F., Kamenev, K. V. & Sokolov, D. A. Structural and magnetic properties of layered $\text{Sr}_7\text{Mn}_4\text{O}_{15}$. *Phys. Rev. B* **64**, 214403 (2001).
- Caimi, G., Degiorgi, L., Berger, H. & Forró, L. Optical evidence for a magnetically driven structural transition in the spin web Cu_3TeO_6 . *Europhys. Lett.* **75**, 496 (2006).
- Kalinin, S. V., Karapetian, E. & Kachanov, M. Nanoelectromechanics of piezoresponse force microscopy. *Phys. Rev. B* **70**, 184101 (2004).
- Karapetian, E., Kachanov, M. & Kalinin, S. V. Nanoelectromechanics of piezoelectric indentation and applications to scanning probe microscopies of ferroelectric materials. *Philos. Mag.* **85**, 1017–1051 (2005).

41. Kalinin, S. V., Eliseev, E. A. & Morozovska, A. N. Materials contrast in piezoresponse force microscopy. *Appl. Phys. Lett.* **88**, 232904 (2006).
42. Eliseev, E. A., Kalinin, S. V., Jesse, S., Bravina, S. L. & Morozovska, A. N. Electromechanical detection in scanning probe microscopy: Tip models and materials contrast. *J. Appl. Phys.* **102**, 014109 (2007).
43. Rodriguez, B. J., Callahan, C., Kalinin, S. V. & Proksch, R. Dual-frequency resonance-tracking atomic force microscopy. *Nanotechnology* **18**, 162–193 (2007).
44. Jesse, S., Kalinin, S. V., Proksch, R., Baddorf, A. P. & Rodriguez, B. J. The band excitation method in scanning probe microscopy for rapid mapping of energy dissipation on the nanoscale. *Nanotechnology* **18**, 733–737 (2007).
45. Jesse, S. & Kalinin, S. V. Band excitation in scanning probe microscopy: sines of change. *J. Phys. D-Appl. Phys.* **44**, 464006 (2011).
46. Lummen, T. T. A. et al. Thermotropic phase boundaries in classic ferroelectrics. *Nat. Commun.* **5**, 3172 (2014).
47. Lajos, L. P. et al. Identification of ferroelectric domain structures in BaTiO₃ for Raman spectroscopy. *Surf. Sci.* **532–535**, 493–500 (2003).
48. Akamatsu, H. et al. Inversion symmetry breaking by oxygen octahedral rotations in the Ruddlesden-Popper nRTiO₄ Family. *Phys. Rev. Lett.* **112**, 187602 (2014).
49. Wu, F., Kan, E., Tian, C. & Whangbo, M.-H. Theoretical analysis of the spin exchange and magnetic dipole–dipole interactions leading to the magnetic structure of Ni₃TeO₆. *Inorg. Chem.* **49**, 7545–7548 (2010).
50. Živković, I., Prša, K., Zaharko, O. & Berger, H. Ni₃TeO₆ — a collinear antiferromagnet with ferromagnetic honeycomb planes. *J. Phys.: Condens. Matter* **22**, 056002 (2010).
51. Xueyun Wang, F.-T. H. & Junjie Yang, YoonSeok Oh, and Sang-Wook Cheong. Interlocked chiral/polar domain walls and large optical rotation in Ni₃TeO₆. *APL Materials* **3**, 076105 (2015).
52. Kim, J. W. et al. Successive Magnetic-Field-Induced Transitions and Colossal Magnetolectric Effect in Ni₃TeO₆. *Phys. Rev. Lett.* **115**, 137201 (2015).
53. Walker, D., Carpenter, M. A. & Hitch, C. M. Some simplifications to multianvil devices for high pressure experiments. *Am. Mineral.* **75**, 1020–1028 (1990).
54. Coelho, A. A. Indexing of powder diffraction patterns by iterative use of singular value decomposition. *J. Appl. Cryst.* **36**, 86–95 (2003).
55. Topas Academic: General profile and structure analysis software for powder diffraction data (Bruker AXS, Karlsruhe, Germany, 2012).
56. Chapon, L. C. et al. Wish: The new powder and single crystal magnetic diffractometer on the second target station. *Neutron News* **22**, 22 (2011).
57. Petricek, V., Dusek, M. & Palatinus, L. Crystallographic Computing System Jana2006: General features. *Z. Kristallogr.* **229**, 345–352 (2014).
58. Campbell, B. J., Stokes, H. T., Tanner, D. E. & Hatch, D. M. ISODISPLACE: a web-based tool for exploring structural distortions. *J. Appl. Crystallogr.* **39**, 607–614 (2006).
59. Croft, M. et al. Systematic Mn d-configuration change in the La_{1-x}Ca_xMnO₃ system: A Mn K-edge XAS study. *Phys. Rev. B* **55**, 8726–8732 (1997).
60. Li, M.-R. et al. Giant magnetoresistance in the half-Mmetallic double-perovskite ferrimagnet Mn₂FeReO₆. *Angew. Chem. Int. Ed.* **54**, 12069–12073 (2015).
61. Denev, S. A., Lummen, T. T. A., Barnes, E., Kumar, A. & Gopalan, V. Probing ferroelectrics using optical second harmonic generation. *J. Am. Ceram. Soc.* **94**, 2699–2727 (2011).
62. Garten, L. M. et al. Relaxor ferroelectric behavior in barium strontium titanate. *J. Am. Ceram. Soc.* **99**, 1645–1650 (2016).
63. Gupta, A. S. et al. Improper inversion symmetry breaking and piezoelectricity through oxygen octahedral rotations in layered perovskite family, LiRTiO₄ (R = rare earths). *Adv. Electron. Mater.* **2**, 1500196–1500196 (2016).
64. Strayer, M. E. et al. Emergent noncentrosymmetry and piezoelectricity driven by oxygen octahedral rotations in n = 2 Dion–Jacobson phase layer perovskites. *Adv. Funct. Mater.* **26**, 1930–1937 (2016).
65. Sen Gupta, A. et al. Competing structural instabilities in the Ruddlesden–Popper derivatives HRTiO₄ (R = rare earths): oxygen octahedral rotations inducing noncentrosymmetry and layer sliding retaining centrosymmetry. *Chem. Mater.* **29**, 656–665 (2017).
66. Gruverman, A., Auciello, O. & Tokumoto, H. Imaging and control of domain structures in ferroelectric thin films via scanning force microscopy. *Annu. Rev. Mater. Sci.* **28**, 101–123 (1998).
67. Gruverman, A. & Kholkin, A. Nanoscale ferroelectrics: processing, characterization and future trends. *Rep. Prog. Phys.* **69**, 2443–2474 (2006).
68. Bonnell, D. A., Kalinin, S. V., Kholkin, A. L. & Gruverman, A. Piezoresponse Force Microscopy: A Window into Electromechanical Behavior at the Nanoscale. *Mrs Bull.* **34**, 648–657 (2009).
69. Balke, N., Bdikin, I., Kalinin, S. V. & Kholkin, A. L. Electromechanical imaging and Spectroscopy of ferroelectric and piezoelectric materials: State of the art and prospects for the future. *J. Am. Ceram. Soc.* **92**, 1629–1647 (2009).
70. Kalinin, S. V., Setter, N. & Kholkin, A. L. Electromechanics on the nanometer scale: Emerging phenomena, devices, and applications. *Mrs Bull.* **34**, 634–642 (2009).

Acknowledgements

This work was supported by the NSF-DMR-1507252 grant. M.R.L. thanks the “One Thousand Youth Talents” Program of China. Use of the NSLS, Brookhaven National Laboratory was supported by the DOE BES (DE-AC02-98CH10886). A.S.G., H.P. and V.G. acknowledge support for them the Penn State NSF-MRSEC Center for Nanoscale Science grant (DMR-1420620). M.R. thanks the Spanish Juan de la Cierva grant FPDI-2013-17582. C.P.G. and J.H. were funded through the Institutional Strategy of the University of Cologne and CRC1238 within the German Excellence Initiative. Experiments at the ISIS Pulsed Neutron and Muon Source were supported by a beam-time allocation from the Science and Technology Facilities Council. P.M. and F.O. acknowledge support from the project TUMOCs. This project has received funding from the European Union’s Horizon 2020 research and innovation programme under the Marie Skłodowska-Curie grant agreements No.645660. PFM experiments were conducted and partially supported (L.C., S.V.K.) at the Center for Nanophase Materials Sciences, which is a US DOE Office of Science User Facility. We are grateful to Prof J.S.O. Evans and Dr A. McLennan for making a long cif Topas macro widely available.

Author contributions

M.-R.L. and M.G. conceived the idea of the project. M.-R.L., M.R., and D.W. prepared the samples. P.W.S. performed the SPXD work. M.C. did the XANES and magnetism analysis. E.E.M., F.O. and P.M. collected the NPD data and analyzed the nuclear magnetic structures. M.-R.L. calculated the magnetostriction-polarization coupling effect. A.S.G., H.P., and V.G. conducted the SHG measurements. Z.D., W.-M.Li, and C.-Q.J. measured the magnetic properties. L.C. and S.V.K. measured and analyzed the PFM part. C.P.G. and J.H. measured the pyroelectric effect and magnetic-field-dependent polarization evolution. M.-R.L. and M.G. co-wrote the paper. All authors commented on the manuscript. M.G. supervised the project.

Additional information

Supplementary Information accompanies this paper at <https://doi.org/10.1038/s41467-017-02003-3>.

Competing interests: The authors declare no competing financial interests.

Reprints and permission information is available online at <http://npg.nature.com/reprintsandpermissions/>

Publisher’s note: Springer Nature remains neutral with regard to jurisdictional claims in published maps and institutional affiliations.



Open Access This article is licensed under a Creative Commons Attribution 4.0 International License, which permits use, sharing, adaptation, distribution and reproduction in any medium or format, as long as you give appropriate credit to the original author(s) and the source, provide a link to the Creative Commons license, and indicate if changes were made. The images or other third party material in this article are included in the article’s Creative Commons license, unless indicated otherwise in a credit line to the material. If material is not included in the article’s Creative Commons license and your intended use is not permitted by statutory regulation or exceeds the permitted use, you will need to obtain permission directly from the copyright holder. To view a copy of this license, visit <http://creativecommons.org/licenses/by/4.0/>.

© The Author(s) 2017